High Performance GaSb/InAs Superlattice Long-Wave Infrared Focal Plane Array

S. D. Gunapala, S. B. Rafol, D. Z. Ting, A. Soibel, J. K. Liu, A. Khoshakhlagh, S. A. Keo, and J. M. Mumolo
Center for Infrared Sensors, Jet Propulsion Laboratory, California Institute of Technology
4800 Oak Grove Drive, Pasadena, CA 91109, USA

Abstract - **We describe the demonstration of a ¼ VGA format long-wavelength infrared focal plane array based on an InAs/GaSb superlattice absorber surrounded by an electron-blocking and a hole-blocking unipolar barrier. An 8.8 µm cutoff focal plane without antireflection coating based on this complementary barrier infrared detector design has yielded noise equivalent differential temperature of 18.6 mK at operating temperature of 80K, with 300 K background and f/2 cold-stop.**

Keywords – superlattices, infrared detectors, focal plane arrays

I. INTRODUCTION

The closely lattice-matched material system of InAs, GaSb, and AlSb, commonly referred to as the 6.1Å material system, has emerged as a fertile ground for the development of new solid-state devices. The flexibility of the system in simultaneously permitting type-I, type-II staggered, and type-II broken-gap band alignments has been the basis for many novel high-performance heterostructure devices in recent years, including the GaSb/InAs type-II superlattice (SL) infrared (IR) detectors. The antimonides based type-II SLs have a great potential in realizing high performance large format highly uniform IR focal plane arrays (FPAs) at lower cost due to the availability of large area epi-ready GaSb substrates and relatively easy III-V materials growth and processing technology compared to its II-VI counterpart. The research in this area has seen rapid progress and many research groups have demonstrated type-II SL detectors and IR FPAs [1-7].

II. CBIRD DEVICE STRUCTURE

The complementary barrier infrared detector (CBIRD) structure needs n on p ROIC as an electrically interface since it provides electrons at the top contact. This CBIRD design consists of a 300-period (44 Å, 21 Å)-InAs/GaSb absorber superlattice (SL) sandwiched between an 80-period (46 Å, 12 Å)-InAs/AlSb hole-barrier (hB) SL on the left and 60-period (22 Å, 21 Å)-InAs/GaSb electro-barrier (eB) SL on the right. The hB SL and eB SL are, respectively, designed to have approximately zero conduction and valence band offset with respect to the absorber SL. The hB SL is doped at $n=1x10^{16}$ cm^{-3} while the absorber SL and eB SL are nominally doped at $p=1x10^{16}$ cm^{-3} [1-8]. $InAs_{0.91}Sb_{0.09}$ adjacent to the eB acts as the V_{DET_COM} contact layer, and the hB SL serves as the top contact layer that is electrically connected to the silicon read out integrated circuit (ROIC). For CBIRD the V_{DET_COM} is at a lower potential relative to the top contact or ROIC. This injects electrons into the ROIC and the operational mode is n on p. The dry etching process was utilized to fabricate the 320 x 256 pixel arrays with 30 µm pixel pitch. FLIR/Indigo two-color direct injection 320x256 pixel format ISC0903 ROIC [10] was used to fabricate FPAs. The detector arrays and ROICs were hybridized using the SET FC-300 flip-chip bonder. After hybridization, the FPAs were backfilled with epoxy and cured overnight. The substrate was completely removed by mechanical lapping followed by the dry etch process all the way down to the etch stop layer.

III. TESTING AND CHARACTERIZATION OF CBIRD FPA

The FPA was cooled down to 78K and 65K for data acquisition at two temperatures. Figure 1 shows the plot of mean external QE as a function of wavelength, which is measured directly from the FPA at 78K, 128 mV bias, and 370 □sec integration time. The maximum QE of 54 % has been achieved for double pass geometry. This is slightly lower than the single element result. The FPA is back illuminated while the single element test device is front-illuminated. The substrate was completely removed and thinned enough to be transparent for IR radiation. The cut-off wavelength is about 8.8 µm, which is at 50% of the peak, and the Full-Width-Half-Maximum (FWHM) is from roughly from 4.4 µm to 8.8 µm. The mean responsivity is 46.2 nV/photon with operability of 97%. The operability is defined as those pixels with responsivity between 20% and 150% of the mean responsivity. The low responsivity can be partially attributed to low ROIC gain which is ~97nV/electron [9].

Figure 2 depicts the dark current density histogram at an operating bias of 128 mV. The integration time was set slightly higher to 490 µsec, which should not affect the dark current estimate. The mean dark current density of ~2.2×10^{-4} A/cm^2 is a factor of 4.4 higher than the mean measured dark current from many single element devices at the same temperature and bias. Estimates show that at 240K background temperature the dark current density is comparable to photocurrent density

from 298K background. The mean dark current density of the large area single element detectors at ~77K was ~ 5 x 10^{-5} A/cm^2. The FPA detector array is not passivated and surface conduction may have contributed to the increase in dark current density.

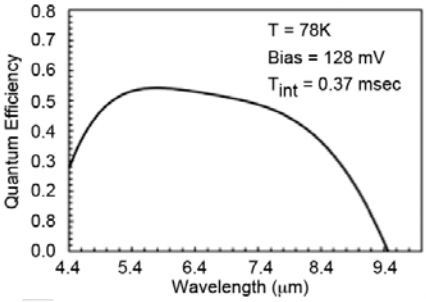

Fig. 1. Quantum efficiency spectrum of long-wavelength superlattice CBIRD device. Quantum efficiency was measured with double-pass geometry.

Excess dark current normally originates from generation-recombination, trap assisted tunneling, and surface leakage [1]. However, when the temperature was lowered to 65K, the mean dark current density decreased to 1.1 x 10^{-4} A/cm^2. This implies that there is a surface leakage in addition to the bulk current. However, the bulk dark current density still dominates considerably and decreases with temperature. The decreasing bulk dark current density as a function of decreasing temperature clearly indicates the absence of trap assisted tunneling assuming the surface leakage current is independent of temperature. The uncorrected spatial non-uniformity (sigma/mean) at 298K blackbody temperature is 5.5%. The temporal NEΔT matrix is numerically evaluated from the relations, $NE\Delta T = \sigma_{Temporal}\Delta T/[Mean(T_H) - Mean(T_L)]$ [6]. The matrices $Mean(T_L)$ and $Mean(T_H)$ are the means evaluated at blackbody temperatures of T_L = 293 K and T_H = 303K. The temporal noise is estimated at 298K using 32 frames, and ΔT ~10K. The experimentally measured NEΔT histograms distributions of the CBIRD FPA at 78K operating temperature, 128 mV bias, and 370 μsec integration time, with blackbody temperature of 298K and an f/2 cold stop, is shown in the Fig. 3. The mean NEΔT of 18.6 mK and 12 mK is achieved at FPA operating temperatures of 78K and 65K respectively. This means that noise has decreased with temperature.

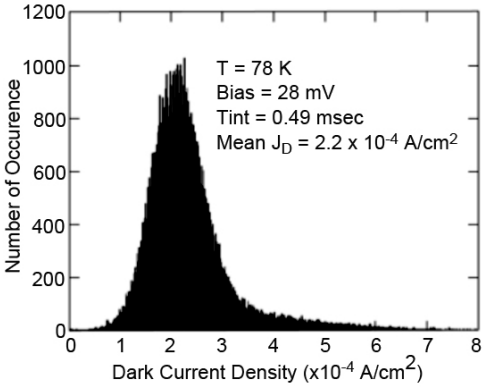

Fig. 2. Dark current of CBIRD at a bias or 128 mV and 78K operating temperature.

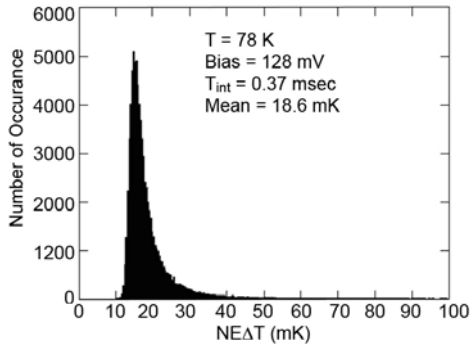

Fig. 3. Measured CBIRD NEΔT histogram operating at 78K, bias of 128 mV and integration time of 370 μsec. The mean NEΔT is 18.6 mK.

IV. MRΔT AND MTF OF CBIRD FPA

In this section we describe the minimum resolvable temperature difference (MRΔT) and MTF measurements. Figure 4(a) and (b) depict MRΔT and MTF plots of an LWIR CBIRD FPA respectively. MRΔT is a subjective measurement of an FPA image using trained human observers. It requires a stable differential temperature between background and a four bar target that will produce a unity signal-to-noise ratio on the display monitor as a function of target spatial frequency [10-12]. This measures thermal sensitivity as a function of spatial resolution defined by the four bar target with aspect ratio of 7:1. The period of the four bar target is varied and the spatial frequency is estimated for each four bar target. At small spatial frequency, the horizontal MRΔT (HMRΔT) and vertical MRΔT (VMRΔT) are slightly lower than the NEΔT value, which is also shown on the MRΔT plot. At higher spatial frequency, it requires a larger temperature difference to generate a contrast between the four bar targets and background. Positive and negative contrast was measured and temperature difference was averaged to eliminate the offset. The four bar target becomes difficult to resolve at 15.89 cycles/mm (which is just below Nyquist frequency ~16.67cycles/mm) in both the vertical and horizontal direction even after moving the target slightly to compensate for the phasing effect and raising the temperature of the background [11]. It is observed that only three bars were apparent instead of four and two of the bars merge into one at a frequency close to Nyquist.

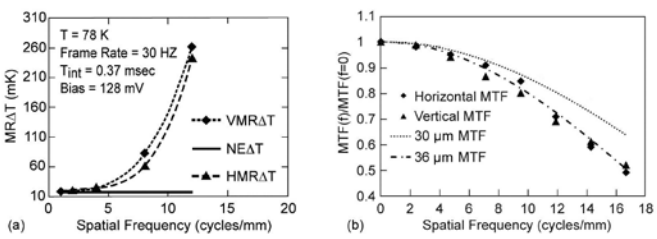

Fig. 4. (a) Minimum Resolvable Temperature Difference (MRΔT) and (b) Modulation Transfer Function (MTF) as a function of spatial frequency measured from 320 x 256 CBIRD FPA operating at 78K, at a bias at 128 mV and integration time of 370 μsec.

MTF technically provides a measure of image resolution or spatial frequency response of the infrared imaging system. It is a measure of how the contrast is transferred from object space to image space as a function of spatial frequency. MTF is inversely related to MRΔT [10]. The ESF is then constructed as previously described. The ESF is numerically differentiated to obtain the LSF. The zero frequency normalized absolute value of the Fourier transform of the LSF is the one dimensional MTF of the system. The lens MTF is removed by dividing the measured MTF with the lens MTF. The plot in Figure 4(b) is MTF(f)/MTF(F=0) of the FPA and electronics in horizontal and vertical orientation.

The higher MTF at low frequency produces better contrast (see Figure 5) and, therefore better images are observed at low spatial frequency. Higher MTF values at high frequency produce good quality images at higher frequency. The horizontal and vertical MTFs at Nyquist frequency based on pixel pitch, a, (= 1/2a, a = 30μm) ~16.67cycles/mm are about ~0.49 and ~0.52, respectively. The Nyquist frequency is well below the optical cut off frequency of ~56.8 cycles/mm based on the 8.8 μm detector cut off wavelength. The loss of MTF can be due to defocusing [10-12 and this defocusing effect is eliminated by acquiring data at the best focus and then collecting data by moving the FPA by ± 50 μm along the optical axis from the best focus location. This is roughly the size of the Airy disk.

The FPA MTF can be separated into the product of two components. The geometric aperture MTF is related to the pixel size and the diffusion MTF related to electro-optical properties [10-12]. The diffusion MTF depends on the diffusion length and geometry. The carrier diffusion degrades high frequency MTF and manifests as crosstalk (or MTF loss). However, the CBIRD pixels are delineated down to the bottom contact and it is expected that no lateral carrier diffusion into the next neighbor can occur. The advantage of delineation is the reduction of cross talk. The disadvantage (in non-planar device structures) is that the fill factor is less than 100%. Shorter wavelengths on the other hand can be absorbed near the top surface and can diffuse to the next neighbor. In CBIRD FPA, the only channel left for the charge carriers to diffuse to an adjacent pixel is through the thin VDET_COM layer.

The geometric aperture MTF can be estimated using a sinc function. Since the pixel is square, the aperture MTF is the same in the horizontal and vertical orientation. For a pixel pitch of 30μm, the CBIRD FPA pixel size, a sinc function describing an aperture MTF is plotted in Fig. 4(b). Smaller pixel size actually improves high frequency MTF since at Nyquist (sampling using FPA pitch) its value is greater than 0.64. The difference between aperture MTF and the measured MTF is the upper limit on the diffusion MTF (crosstalk) since other MTF components such as electronic and other effects are not known completely as well as surface recombination. The ROIC crosstalk is small, ~ 0.1% by design. At Nyquist frequency, the difference between measured horizontal/vertical and the ideal MTF is ~0.14, but at low frequencies the difference is small. The MTF loss is basically an effective increase of the pixel size. The geometric aperture MTF function decreases with increasing pixel size and frequency. Thus detectors can be viewed as an overlapping Gaussian-like array. For example, for horizontal and vertical MTF data in Fig. 4(b) the pixel size that will closely match the MTF data is roughly ~ 36 m which is larger than the pitch. Imagery was performed at 78K FPA operating temperature and Fig. 14 shows outside natural scenery. The image quality of the natural scene attests to the very good MTF behavior at low and high frequencies. This FPA gave good images, with more than 97% of the pixels operable. Video images were taken at a frame rate of 30 Hz and integration time of 0.37 msec.

Fig. 5. Outside images taken with the long-wavelength infrared CBIRD superlattice focal plane array. The FPA is operated at 78K with NEΔT of 18.6 mK with f/2 optics at 300K background. This image show good quality reproduction of low and high spatial frequency.

V. CONCLUSION

A 320x256 format LWIR CBIRD FPA has been demonstrated with 18.6 mK NEΔT for 300K background with f/2 cold stop at 78K FPA operating temperature. The horizontal and vertical MTFs of this pixel fully delineated CBIRD FPA at Nyquist frequency are 49% and 52%, respectively.

ACKNOWLEDGMENT

The authors thank S. Khanna, T. Cwik, R. Liang, M. Herman and E. Kolawa of JPL, R. Stephan of the Game Changing Technology Division at the NASA Office of the Chief Technologist, and M. Tidrow of the U.S. Army Night Vision Electronics Sensor Directorate. The research described in this paper was carried out at the Jet Propulsion Laboratory, California Institute of Technology, through an agreement with the National Aeronautics and Space Administration. Copyright 2012 California Institute of Technology.

REFERENCES

[1] David Z. Ting, Cory J. Hill, Alexander Soibel, Sam A. Keo, Jason M. Mumolo, Jean Nguyen, Sarath D. Gunapala, Appl. Phys. Lett. Vol. 95, pp. 023508, 2009.

[2] S. Maimon and G. W. Wicks, nBn detector, an infrared detector with reduced dark current and higher operating temperature, *Appl. Phys. Lett*. **89**(15) 151109 (2006).

[3] P. Klipstein, Depletion-less photodiode with suppressed dark current and method for producing the same, United States Patent No: US 7,795,640 B2 (Sep 14, 2010).

[4] Philip Klipstein, Olga Klin, Steve Grossman, Noam Snapi, Barak Yaakobovitz, Maya Brumer, Inna Lukomsky, Daniel Aronov, Michael Yassen, Boris Yofis, Alex Glozman, Tal Fishman, Eyal Berkowicz, Osnat Magen, Itay Shtrichman, and Eliezer Weiss, XBn barrier detectors for high operating temperatures, Proc. SPIE 7608, 76081V (2010).

[5] F. Fuchs, U. Weimer, W. Pletschen, J. Schmitz, E. Ahlswere, M. Walter, J. Wagner, and P. Koidl, High performance InAs/$Ga_{1-x}In_xSb$ superlattice infrared photodiodes, *Appl. Phys. Lett.* **71**(22), 3251 (1997).

[6] P.-Y. Delaunay, B. M. Nguyen, D. Hoffman, E. K.-W. Huang, M. Razeghi, Background Limited Performance of Long Wavelength Infrared Focal Plane Arrays Fabricated From M-Structure InAs–GaSb Superlattices, *IEEE J. Quant. Electron*. **45**(102), 157-162 (2009).

[7] H. S. Kim, E. Plis, J. B. Rodriguez, G. D. Bishop, Y. D. Sharma, L. R. Dawson, S. Krishna, J. Bundas, R. Cook, D. Burrows, R. Dennis, K. Patnaude, A. Reisinger, and M. Sundaram, Mid-IR focal plane array based on type-II InAs/GaSb strain layer superlattice detector with nBn design, *Appl. Phys. Lett*. **92**(18), 183502 (2008).

[8] S. D. Gunapala, D. Z. Ting, C. J. Hill, J. Nguyen, A. Soibel, S. B. Rafol, S. A. Keo, J. M. Mumolo, M. C. Lee, J. K. Liu, and B. Yang, IEEE Photonics Technology Letters, Vol. 22, pp. 1856-1858, 2010.

[9] B. Simolon, A. Aziz, R. Hansen, E. Kurth, S. Lam, S. Petronio, and J. Woolaway, Infrared Physics & Technology

[10] G. C. Holst, The Infrared Electro-Optical Systems Handbook, M. C. Dudzik, Ed. Bellingham, WA: SPIE, 1993.

[11] Glenn D. Boreman, "Modulation Transfer Function in Optical and Electro-Optical Systems", SPIE Press, 2001.

[12] S. D. Gunapala, S. V. Bandara, J. K. Liu, C. J. Hill, S. B. Rafol, J. M. Mumolo, J. T. Trinh, M. Z. Tidrow, and P. D. LeVan, Semicond. Sci. Technol., Vol. 20, pp. 473-480, 2005.